Nanotechnol. Environ. Eng. (2017) 2:17
https://doi.org/10.1007/s41204-017-0028-5

ORIGINAL PAPER

Facile synthesis of SiO_2@TiO_2 crystallite photocatalysts with enhanced interaction level and high light absorption efficiency

Zhenting Bo[1] · Rulin Dong[1] · Changchun Jin[1] · Zhidong Chen[1]

Received: 24 July 2017 / Accepted: 5 September 2017 / Published online: 11 September 2017

Abstract SiO_2@TiO_2 crystallite photocatalysts with TiO_2 crystallite core and porous amorphous SiO_2/TiO_2 shell were synthesized as photocatalyst by one-pot hydrothermal process using tetrabutyl titanate (TBOT) complex and ethyl orthosilicate (TEOS) as Ti and Si sources, respectively. The synthesized SiO_2@TiO_2 crystallite photocatalysts were characterized by transmission electron microscopy, X-ray diffraction pattern, UV–Vis diffuse reflectance spectrum and N_2 adsorption–desorption isotherm. The interaction between TiO_2 and SiO_2, which is associated with photocatalytically active centers, is significantly improved through an enlargement in the interfacial area and the optimization of SiO_2 fraction. The SiO_2 modification does not lower the light absorption efficiency of TiO_2 crystallite core owning to the low reflectivity of porous SiO_2/TiO_2 shell but endows the photocatalyst with easy separation behavior from aqueous solution. Furthermore, the reciprocal inhibition in volume shrinkage of TBOT complex- and TEOS-derived gel networks, as a consequence of mineralization asynchronism, increases the specific surface area and pore volume of the formed SiO_2/TiO_2 shell. The enhanced photocatalytic activity of SiO_2@TiO_2 crystallite photocatalysts by SiO_2 modification is mainly ascribed to an increase in the interaction level, the high light absorption efficiency of SiO_2@TiO_2 crystallite photocatalysts and an enlargement in specific surface area of SiO_2/TiO_2 shell.

✉ Rulin Dong
dongrl@cczu.edu.cn

[1] Jiangsu Key Laboratory of Advanced Catalytic Materials and Technology, Changzhou University, Changzhou 213164, People's Republic of China

Keywords Hydrothermal process · TiO_2 crystallite · SiO_2 · Light absorption · Adsorption kinetics · Photocatalysis

Introduction

Semiconductor TiO_2 has been extensively studied as photocatalyst for the degradation of organic pollutant in water or air due to its chemical and physical stability, superior photocatalytic oxidation ability, easy availability, low cost and nontoxicity [1–3]. The mechanism of TiO_2-based photocatalytic reaction [4, 5] can be described as follows: Electrons in the valence band of TiO_2 absorb photon energy and get excited to the conduction band with the formation of positive holes in the valence band. The excited electrons can react with adsorbed O_2 to form superoxide radical anions ($\cdot O_2^-$), while the holes in valence band react with adsorbed OH^- or H_2O to form highly reactive hydroxyl radicals (·OH) that has strongly oxidizing power for the degradation of recalcitrant organic compounds but has short lifetime (usually 10^{-9} s). Photo-induced hydroxyl radical is regarded as the major oxidative species in photocatalytic degradation reaction and exists in two forms, i.e., free ·OH and surface-bonded ·OH. Xiang et al. [4] measured the hydroxyl radical yield of various photocatalysts by photoluminescence technique and proposed a concept of hydroxyl radical index for evaluating the activity of photocatalyst. However, some critical drawbacks obstruct the practical application of TiO_2 in the degradation of organic pollutant in water and air. The ineffective charge carrier separation as a consequence of shorter carrier lifetime is the ultimate crisis for TiO_2 photocatalyst. Besides, light-induced charge carrier pair recombination also occurs in parallel during photocatalytic process. Moreover, TiO_2 absorbs UV light that is the tiny

portion of solar spectrum but has meager response to visible light due to a wide band gap of TiO_2 [6, 7]. Fortunately, many novel approaches like doping with impurities [8–10], noble metal deposition [11, 12], sensitizing with narrow band gap absorption materials [13, 14] and hydrogenation process [15, 16] have been found to be effective in enabling visible light absorption, while several inventive techniques such as heterostructuring with other semiconductors [17, 18], integrating with carbon nanostructures [19, 20], designing with exposed reactive facets [12, 21] and hierarchical morphologies [22, 23] have been developed to improve structural stability and charge carrier separation kinetics.

Porous amorphous SiO_2 nanomaterials are normally employed as a carrier for TiO_2 nanoparticles (NPs) due to their compatibility for TiO_2 deposition, and their high specific surface area that endows TiO_2 with an ability of enriching pollutant molecules in aqueous medium and gaseous phase onto catalyst surface. For instance, Wu et al. [5] synthesized core–shell structural SiO_2/TiO_2 NPs using monodispersed teardrop-shaped silica NPs as carrier by sol–gel method. Liu [24] prepared mesoporous SiO_2 aerogel/W_xTiO_2 nanocomposites by a hydrothermal deposition method using SiO_2 aerogel as a carrier. Besides the increase in specific surface area, the photocatalytic activity of TiO_2 can also be improved by the SiO_2 modification as the interaction between the counterparts increases the concentration of photocatalytically active centers [5, 25]. In order to increase the interfacial area between TiO_2 and SiO_2, Resende et al. [26] introduced SiO_2 colloidal particle into mesoporous TiO_2 microspheres by an ultrasonic treatment of TiO_2 microspheres in SiO_2 sol and a subsequent heat treatment of the microspheres. In consideration of the absorption and scattering effect of carrier to the incident light, TiO_2 NPs are normally deposited on the surface of SiO_2 carrier so that TiO_2 NPs can be adequately irradiated. However, only a small portion of the surface of TiO_2 NPs in such carrier-supported TiO_2 is utilized in forming the interface with SiO_2, and excessive deposition may easy lead to the formation of agglomeration of TiO_2 crystallite on the carrier. This provides a potential challenge in further improving the heterostructure to increase the photocatalytic activity of TiO_2. Moreover, because most of the approaches for the synthesis of SiO_2-supported TiO_2 photocatalysts need at least two steps including the preparation of SiO_2 carrier and the deposition of TiO_2 NPs, a simple one-pot approach would be desired for the synthesis of SiO_2/TiO_2 photocatalyst.

In the present work, $SiO_2@TiO_2$ crystallite photocatalysts with TiO_2 crystallite core and porous SiO_2/TiO_2 shell were synthesized by one-pot hydrothermal route using tetrabutyl titanate (TBOT) and ethyl orthosilicate (TEOS) as the precursors of TiO_2 and SiO_2, respectively. In a quest to achieve a comparable hydrolysis reaction rate of TBOT with that of TEOS, TBOT was allowed to react with acetylacetone (ACAC), and the resultant TBOT complex with a moderate hydrolysis rate was used in the subsequent hydrothermal reaction. The synthesized $SiO_2@TiO_2$ crystallite photocatalysts have large interfacial area between the counterparts because the catalytically active TiO_2 crystallites are wrapped with porous amorphous SiO_2/TiO_2 shell. The results indicate that the porous SiO_2/TiO_2 shell not only does not hinder the light absorption of TiO_2 crystallite but also maintains superior light absorption property of the $SiO_2@TiO_2$ crystallite photocatalysts even in the presence of agglomeration due to its low reflectivity. The adsorption capacity and photocatalytic activity of the $SiO_2@TiO_2$ crystallite photocatalysts were measured and compared with those of pure TiO_2 nanoparticles through the degradation of methylene blue in aqueous solution under UV light irradiation.

Materials and methods

Materials

Tetrabutyltitanate ($Ti(OBu^n)_4$, TBOT), tetraethoxysilane ($Si(OC_2H_5)_4$, TEOS), methylene blue (MB), cyclohexane and ethanol were purchased from Sinopharm Chemical Reagent Co., LTD. Acetylacetone (ACAC) was purchased from Jiangsu Qiangsheng Chemical Engineering Co., LTD. All the chemicals were of analytical grade and used without further purification.

Preparation of $SiO_2@TiO_2$ crystallite

TBOT complex prepared by mixing 5 mL of TBOT with 2 mL of ACAC was dispersed in a mixed solvent containing 40 mL of ethanol and 2 mL of cyclohexane under magnetic stirring. Then, 40 mL of distilled water was slowly added into the solution and the stirring was maintained for 30 min. Thereafter, a certain amount of TEOS was added into the solution according to the desired molar fraction ($n_{Si}/(n_{Ti} + n_{Si}) = x\%$) of the final $SiO_2@TiO_2$ crystallite photocatalysts After being stirred for 30 min, the solution was equally transferred into four Teflon-lined autoclaves with a volume capacity of 25 mL. The autoclaves containing reactant solutions were sealed, heated at 150 °C for 10 h, and left to cool naturally to ambient temperature. The synthesized $SiO_2@TiO_2$ crystallite photocatalysts were washed with distilled water and ethanol in sequence, and finally dried at 100 °C for 2 h in a drying oven. Pure TiO_2 NPs were also prepared as a reference by the similar procedure without adding TEOS in the solution. The obtained $SiO_2@TiO_2$ crystallite

photocatalysts were assigned as TSx, where T and S represent TiO_2, SiO_2, respectively, and x represents the molar fraction of SiO_2.

Characterization of SiO_2@TiO_2 crystallite

The morphology and microstructure of the pure TiO_2 and SiO_2@TiO_2 crystallite photocatalysts were characterized by a transmission electron microscope (TEM, JEM-2100, JEOL, Japan). Disk-shaped specimens (diameter: 10 mm) of TS30, prepared under a pressure of 20 MPa, were used to measure the SiO_2 fraction on an energy-dispersive X-ray (EDX) spectrometer attached to a scanning electron microscopy (SEM, JSM-6360LA, JEOL, Japan). X-ray diffraction analysis was carried out by a X-ray diffractometer (XRD, D/Max2500 Rigaku, Japan) with Cu K radiation ($\lambda = 0.15406$ nm) at a scan rate of $0.1^\circ\ s^{-1}$ to determine the crystalline phase in SiO_2@TiO_2 crystallite photocatalysts and the crystalline particle size of TiO_2. The accelerating voltage and applied current were 40 kV and 100 mA, respectively. Nitrogen adsorption–desorption isotherms at 77 K were recorded on an ASAP2010C Micromeritics volumetric adsorption analyzer and were used to analyze the texture of SiO_2@TiO_2 crystallite photocatalysts. UV–Vis diffuse reflectance spectra (DRS) of the pure TiO_2 and SiO_2@TiO_2 crystallite photocatalysts were recorded in the wavelength range of 200–800 nm by a UV–Vis diffuse reflectance spectrometer (UV-3600 Shimadzu, Japan) using barium sulfate as reference. Fifty milligrams of the SiO_2@TiO_2 crystallite photocatalysts was calcined at 500 °C for 30 min to remove the possible organic residuals in samples and then used in the measurement.

Photocatalytic activity of SiO_2@TiO_2 crystallite

Adsorption of MB

Ten milligrams of SiO_2@TiO_2 crystallite photocatalysts was added into a beaker containing 40 mL of MB solution with a concentration of 10 mg L^{-1}. The solution was monitored by measuring the absorption spectrum of MB solution at a certain time interval using the 756S UV–Vis spectrophotometer during the adsorption process. The adsorption capacity (q_t, mg g^{-1}) is determined as follows:

$$q_t = 1000 \times (1 - A_t/A_0) \times C_0 \times V/m_p \quad (1)$$

where C_0 and A_0 are the concentration and absorbance of initial MB solution, respectively, C_t and A_t are the concentration and absorbance of MB solution, and q_t the adsorption capacity of photocatalyst after t h adsorption, respectively, and V and m_p are the volume of solution and the mass of photocatalyst, respectively.

Photocatalytic degradation of MB

After the adsorption process described in "Adsorption of MB" section is finished, the beaker containing photocatalyst and MB solution was exposed to UV light emitted by a 30-W quartz UV modulator tube. The vertical distance between tube and the surface of solution is set at 10 cm. The absorption spectrum of MB solution was recorded during the irradiation at a certain time interval, and the measured data were fitted with first-order reaction kinetic equations. Reaction rate based on the slope of fitted regression line was used to evaluate the photocatalytic activity of SiO_2@TiO_2 crystallite photocatalysts.

Results and discussion

Microstructure of SiO_2@TiO_2 crystallite

Figure 1 displays the TEM images of TS0, TS20 and TS40. The TS0 particles appear a tetragonal bipyramidal morphology, and the particle size is estimated to be 10 nm as shown in Fig. 1a. In general condition, anatase TiO_2 crystallite grows with the preferential exposure of {101} facet with a lower surface energy, which leads to the formation of tetragonal bipyramidal TiO_2 nanocrystals. It was reported that fluorine-containing species can favor the preferential exposure of {001} facet of anatase and thus the formation of TiO_2 nanoplate [6, 12, 21]. TS20 and TS40 without regular TiO_2 crystal shape show mullein-like morphology as shown in Fig. 1b, c. This indicates the SiO_2 modification on TiO_2 crystallites and implies that the interaction between SiO_2 and TiO_2 crystallite probably weakens the preferential growth of lattice plane. The interplanar spacing of the lattice plane shown in Fig. 1d is measured to be 0.350 nm, corresponding to the (101) crystallographic plane of anatase TiO_2. Also, Fig. 1d clearly shows an amorphous covering on an exposed crystallographic plane of TiO_2 crystallite, which confirms the formation of core–shell microstructure. N_2 adsorption–desorption isothermals of SiO_2@TiO_2 crystallite photocatalysts described latter suggest that the formed amorphous covering on TiO_2 crystalline particle is not pure SiO_2 but porous SiO_2/TiO_2 shell.

The XRD patterns of TS0–TS50 shown in Fig. 2a are similar to one another. All the diffraction peaks in the patterns were identified to be anatase TiO_2 (JCPDS, No. 21-1272) and no other diffraction peak was detected, which indicates that the formed SiO_2 phase is amorphous and that no other TiO_2 crystallographic phase exists in the products. As an evidence of SiO_2 modification, an amorphous SiO_2-induced bump arises at $2\theta = 25.3^\circ$ for the patterns of SiO_2@TiO_2 crystallite photocatalysts and its intensity

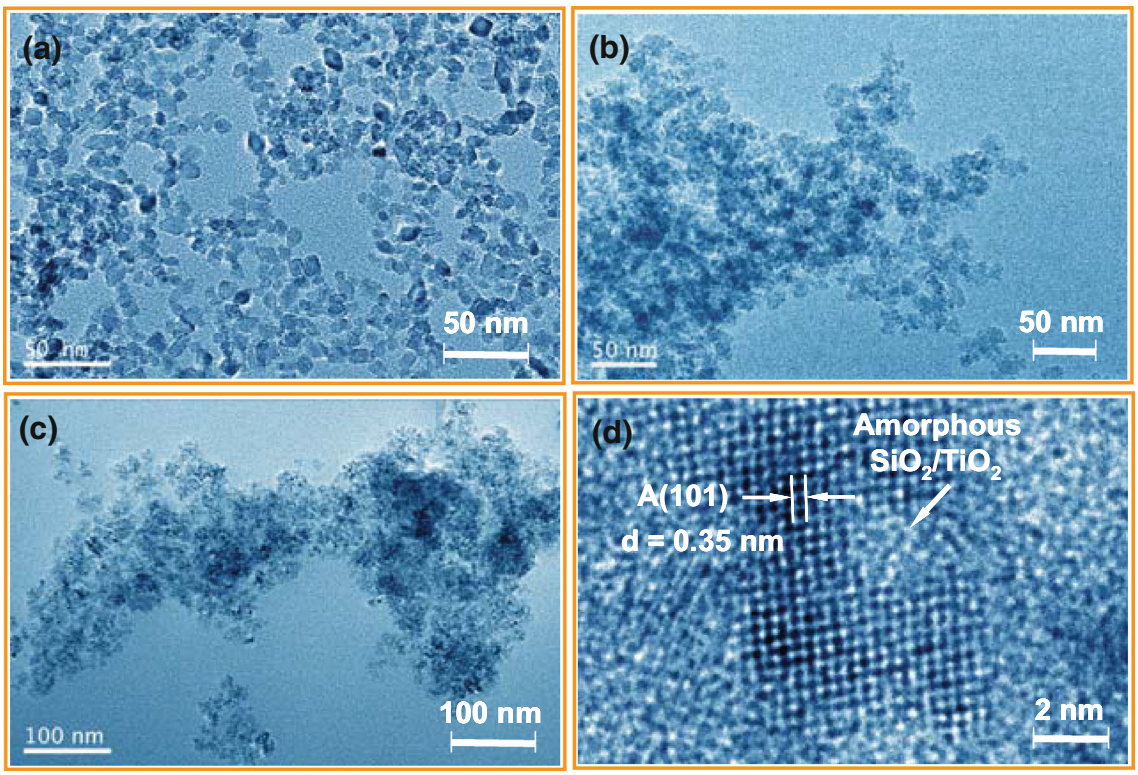

Fig. 1 TEM images of TS0 (**a**), TS20 (**b**) and TS40 (**c**) and high-resolution TEM image of TS40 (**d**)

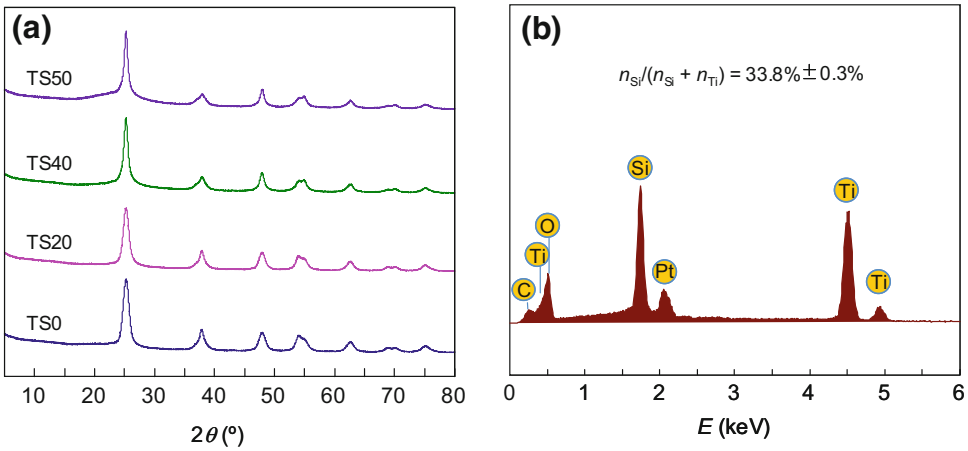

Fig. 2 XRD patterns of TS0–TS50 (**a**) and EDX spectra measured from TS30 disk specimen (**b**)

increases with the increase of SiO_2 fraction. The crystalline particle size for TS0, TS10, TS20, TS30, TS40 and TS50 was calculated to be 9.20, 9.54, 11.00, 12.24, 13.38 and 13.45 nm, respectively, based on Scherrer formula [27] (Eq. 2) and the (101) peaks of anatase TiO_2.

$$D_{(hkl)} = K\lambda/(b\cos\theta) \quad (2)$$

where, $D_{(hkl)}$ is the estimated crystalline particle size, λ is the wavelength of incident X-ray (Cu Kα, 0.154056 nm), θ and β are the diffraction angle and full width at half maximum (FWHM) of (hkl) characteristic peak of TiO_2, respectively, and K *is* Scherrer constant (0.89). Figure 2b depicts the EDX spectrum of TS30. The spectrum shows element response signals of Ti, Si, O, Pt and C. The Pt response signal is caused by Pt film coated on the surface of specimen before measurement. C response signal may be originated from the small amount of residual organic group. The Si atom fraction of $n_{Si}/(n_{Ti} + n_{Si})$ is measured to be 33.8% ± 0.3%. Because the characteristic X-ray signal of element comes from a very thin surface layer of sample and weakens with the increase of depth, the measured Si atom fraction is slightly high than the theoretical value of 30%, which in turn confirms the formation of SiO_2/TiO_2 modification layer on TiO_2 crystalline particles.

Figure 3a shows the UV–Vis diffuse reflectance spectra of TS0–TS50. Because amorphous SiO_2/TiO_2 shell in the composites has no absorption in the wavelength range of 200-800 nm, the strong absorption band located around $\lambda = 300$ nm is originated from the excitation of elections from the valence band to conduction band of TiO_2. The absorbance of $SiO_2@TiO_2$ crystallite photocatalysts in the wavelength 200–400 nm increases with the increase of SiO_2 fraction from 0 to 40% even the absolute amount of TiO_2 crystallite in sample decreases. This indicates a low reflectivity of $SiO_2@TiO_2$ crystallite powder compact as compared with that of pure TiO_2 powder compact because the high light transmittance of SiO_2/TiO_2 shell benefits the light absorption of TiO_2 crystallites under the surface of powder compact. Actually, SiO_2/TiO_2 composite film has been extensively studied as anti-reflection surface material in solar devices due to its high light transmittance [28, 29]. The above result means that our $SiO_2@TiO_2$ crystallite photocatalysts have superior light absorption property even in the presence of agglomeration. The band gap energy can be estimated from UV–Vis diffuse reflectance spectrum according to the equation of $(\alpha h\upsilon) = A(h\upsilon\text{-}E_g)^2$ [30], where $h\upsilon$ is photon energy, α is molar absorption coefficient and can be calculated with reflectance (R) as follows [31]:

$$\alpha = (1 - R)^2/(2R) \quad (3)$$

Figure 3b shows the plot of $(\alpha h\upsilon)^{0.5}$ versus $h\upsilon$ for TS0–TS50 photocatalysts. The estimated band gap energies for TS0, TS10, TS20, TS30, TS40 and TS50 are 3.176, 3.202, 3.226, 3.267, 3.275 and 3.275 eV, respectively. That is, the band gap energy of TiO_2 increases with the increase of SiO_2 fraction and reaches a constant value at 40% SiO_2, which reveals the formation of Ti–O–Si bond and that the amount of Ti–O–Si bond increases with the increase of SiO_2 fraction. In our previous research [32], the formation of TiO_2/SiO_2 shell as well as Ti–O–Si bond in TiO_2/SiO_2 microspheres derived from the same precursors was discussed in detail based on thermogravimetric analysis for the intermediates and X-ray photoelectron spectroscopy analysis for the microspheres. In this regard, the increase in TiO_2 band gap energy can be used as an index of interaction level for TiO_2/SiO_2 composite.

Figure 4 illustrates the formation mechanisms of pure TiO_2 and $SiO_2@TiO_2$ crystallite photocatalysts. An increase in temperature of the solution during the hydrothermal process decreases the compatibility of TBOT complex with the solvent and leads to the formation of dispersed colloidal droplets of TBOT complex. Meanwhile, the hydrolysis and condensation reactions of free-TBOT complex as well as TEOS molecules in the solvent result in the formation of polymeric gel anchored on the surface of colloidal droplets. The colloidal droplet and polymeric gel layer undergo mineralization and finally transform into TiO_2 crystallite core and amorphous SiO_2/TiO_2 shell, respectively, as shown in Fig. 4b. As the growth of TiO_2 crystallite is localized within the colloidal droplets, it would not be inhibited by SiO_2. Moreover, the grafted TEOS induces a decrease in the stability of colloidal droplet and thus an increase in the colloidal droplet size. As a consequence, the higher the TEOS concentration, the larger TiO_2 crystallite is formed. In the case without TEOS in the solution, the dispersed colloidal droplets crystallize into pure anatase TiO_2 crystalline particles as shown in Fig. 4a.

Figure 5 shows the N_2 adsorption–desorption isotherms of typical products. The adsorption isotherms shown in Fig. 5 were identified to be IV type according to IUPAC classification, indicating a typical mesoporous material. The adsorption volume at the same N_2 pressure increases with the increase of SiO_2 fraction, especially for TS30 and TS40. The textural parameters measured by N_2 adsorption–desorption isotherm are summarized in Table 1. The specific surface area of $SiO_2@TiO_2$ crystallite photocatalysts significantly increases with the increase of SiO_2 fraction because the hydrothermally produced amorphous SiO_2 possesses a high surface area. It is interesting to note that the pore volume and pore size increase, reach a maximum value at 30%SiO_2 and then decrease with the

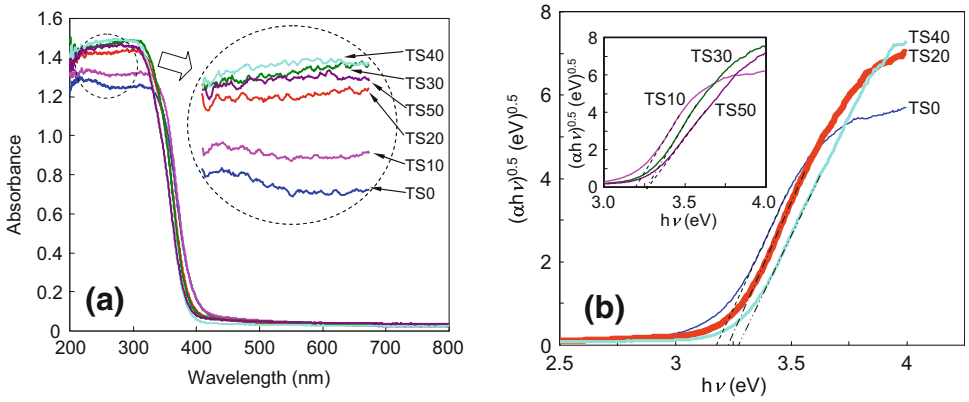

Fig. 3 UV–Vis diffuse reflectance spectra of TS0–TS50 (**a**) and plot of $(\alpha h\upsilon)^{0.5}$ versus $h\upsilon$ (**b**)

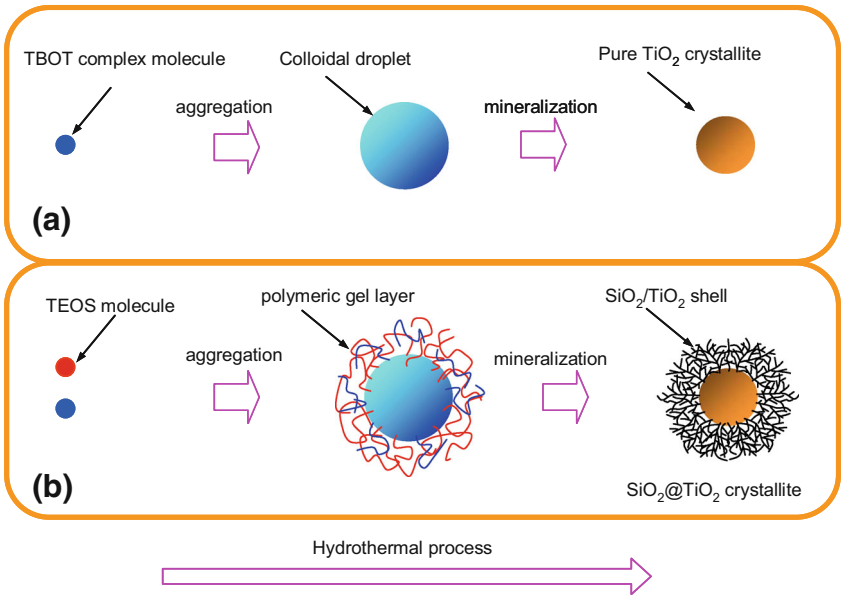

Fig. 4 Schematic illustration for the formation of pure TiO_2 crystallite (**a**) and SiO_2@TiO_2 crystallite (**b**)

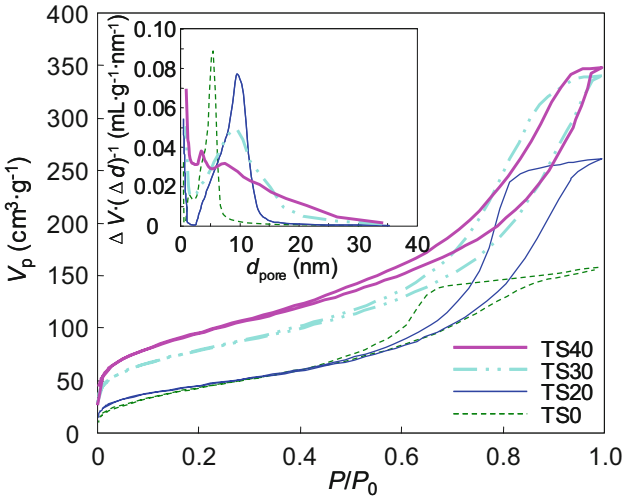

Fig. 5 N_2 adsorption–desorption isotherms and pore size distributions (*inset*) of typical products

Table 1 Textural parameters of TiO_2/SiO_2 measured by N_2 adsorption–desorption isotherm

Sample	S_{BET} (m^2 g^{-1})	V_{pore} (cm^3 g^{-1})	d_{pore} (nm)
TS0	169.86	0.224	4.86
TS20	164.53	0.391	7.39
TS30	280.18	0.486	7.80
TS40	338.11	0.477	7.32

further increase of SiO_2 fraction. The enlarged specific surface area, pore volume and pore size, indicating a looser SiO_2/TiO_2 shell on the surface of TiO_2 crystalline particles, are resulted from a reciprocal inhibition effect in volume shrinkage of TBOT complex- and TEOS-derived gel networks. The reciprocal inhibition effect can be described as follows: Due to the further hydrolysis and condensation reactions, the TBOT complex- and TEOS-derived polymeric gel shell is gradually mineralized with volume shrinkage during the hydrothermal process. On the one hand, the volume shrinkage of TBOT complex gel network first occurs, but a further shrinkage is hindered by TEOS gel network because of the higher hydrolysis activity of TBOT complex compared with that of TEOS. On the other hand, the subsequent volume shrinkage of TEOS gel network is in turn suppressed by the mineralized TBOT complex gel. As a result, large surface area and pore volume are formed in the SiO_2/TiO_2 shell due to the reciprocal inhibition effect that originated from mineralization asynchronism between TBOT complex and TEOS. It is no doubt that strong reciprocal inhibition effect can be achieved at an appropriate ratio of TBOT complex to TEOS in the polymeric gel layer. Accordingly, the pore volume and pore size of SiO_2@TiO_2 crystallite photocatalysts have a maximum value at 30%SiO_2. Suppose that the shell is a pure SiO_2, the pore volume would continuously increase with the increase of SiO_2 fraction. In fact, a decrease in the pore volume of SiO_2@TiO_2 crystallite photocatalysts is observed at an excessively high SiO_2 fraction of 40%. This also confirms the concept of the formation of SiO_2/TiO_2 shell. As compared with that of TS0, a broadened pore size distribution of TS20–TS40 shown in inset of Fig. 5 also indicates the reciprocal inhibition effect and the formation of loose SiO_2/TiO_2 shell on TiO_2 crystalline particles. Furthermore, the enlarged specific surface area and pore volume mean the formation of large number of microchannels through which the reactants and resultants can successfully migrate.

Photocatalysis of SiO_2@TiO_2 crystallite

Adsorption kinetics

Figure 6a, b shows the temporal changes in the absorption spectra of MB solutions with representative TS0 and TS40 during adsorption process. MB exhibits a strong absorption band at 664 nm due to heteropolyaromatic linkage, with a shoulder locating at 292 nm due to benzene ring [20]. As seen in Fig. 6a, no obvious decrease in absorption intensity of MB solution is observed for TS0 during adsorption process. However, the absorption intensity of MB solution distinctly decreases for TS10–TS50 as the adsorption time interval increases. This indicates that the SiO_2 modification leads to a change in the microstructure and an enhancement in the adsorption capacity of SiO_2@TiO_2 crystallite photocatalysts. In order to well understand the adsorption kinetics, we matched the adsorption data with pseudo-first-order (Eq. 4), pseudo-second-order (Eq. 5) and intraparticle diffusion (Eq. 6) adsorption kinetic equations [33], respectively. The fitted parameters and regression coefficients (R^2) are summarized in Table 2.

(1) Pseudo-first-order adsorption kinetic equation:

$$\ln(q_e - q_t) = \ln q_e - k_1 t \quad (4)$$

where k_1 is the pseudo-first-order adsorption rate constant, and q_t and q_e are the adsorption capacity of photocatalyst at adsorption time t and at adsorption equilibrium, respectively.

(2) Pseudo-second-order adsorption kinetic equation:

$$t/q_t = 1/\left(k_2 q_e^2\right) + t/q_e \quad (5)$$

where k_2 is the pseudo-second-order adsorption rate constant.

(3) Intraparticle diffusion adsorption kinetic equation:

$$q_t = k_p q_e^{0.5} + C \quad (6)$$

where k_p is the intraparticle diffusion rate constant, and C is a constant related to the boundary layer thickness.

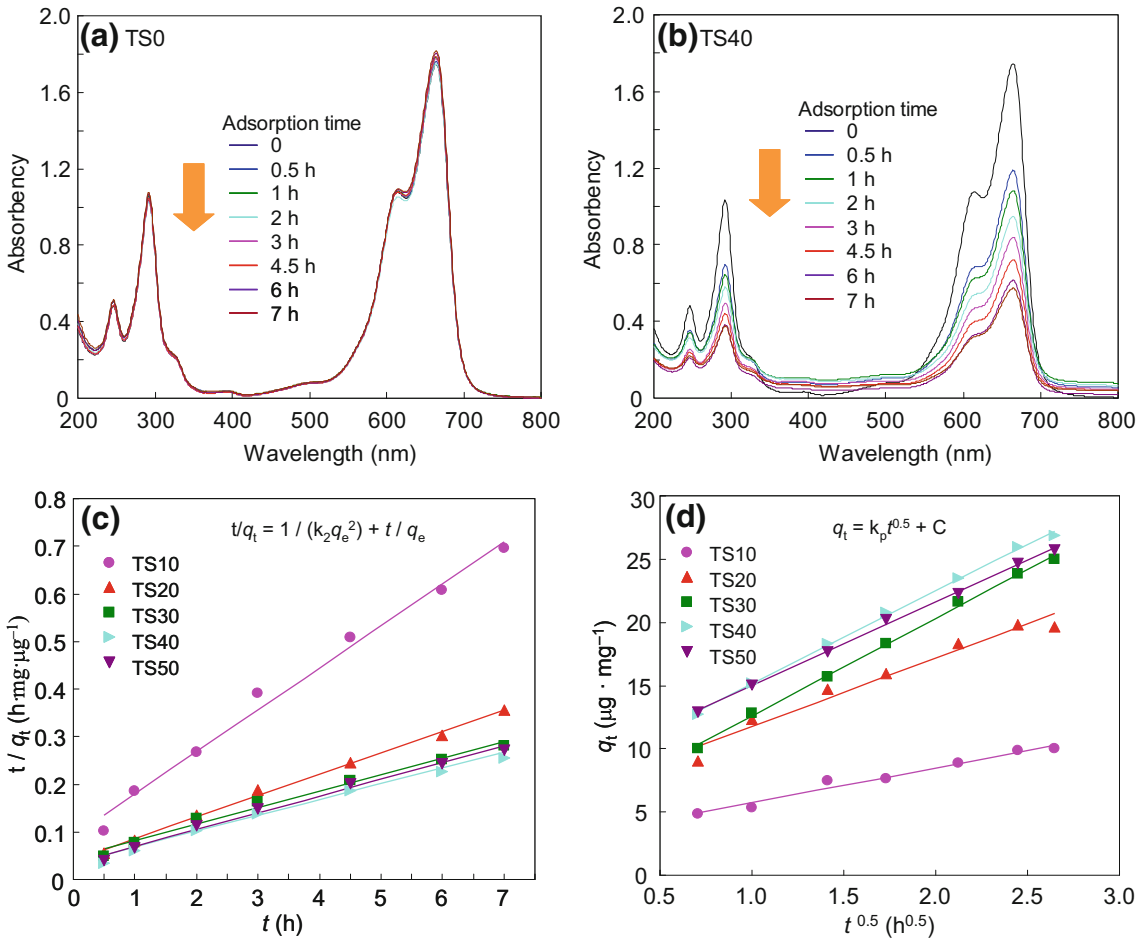

Fig. 6 Temporal changes in the absorption spectra of MB solutions with TS0 (**a**) and TS40 (**b**) during adsorption process and the plots of pseudo-second-order (**c**) and intraparticle diffusion (**d**) adsorption kinetic equations

Table 2 Fitted parameters by the adsorption kinetic equations for MB adsorption on TS10–TS50

Sample	Pseudo-first order			Pseudo-second order			Intraparticle diffusion	
	$\ln(q_e - q_t) = \ln q_e - k_1 t$			$t/q_t = 1/(k_2 q_e^2) + t/q_e$			$q_t = k_p t^{0.5} + C$	
	R^2	q_e (mg g^{-1})	k_1 (h^{-1})	R^2	q_e (mg g^{-1})	k_2 (g mg^{-1} h^{-1})	R^2	k_p (mg g^{-1} h$^{-0.5}$)
TS10	0.9198	9.160	0.5711	0.9891	11.31	0.08541	0.9786	2.773
TS20	0.9641	15.61	0.5407	0.9957	22.17	0.05034	0.9641	5.413
TS30	0.9730	22.37	0.4615	0.9855	29.07	0.02497	0.9980	7.750
TS40	0.9594	22.46	0.4875	0.9897	30.03	0.03177	0.9983	7.341
TS50	0.9794	14.13	0.5353	0.9898	28.33	0.03687	0.9982	6.618

The adsorption capacity is closely related to the microstructure of SiO_2@TiO_2 crystallite photocatalysts. As the SiO_2 fraction increases, the MB adsorption capacity increases due to an increase in the specific surface area and pore volume of SiO_2@TiO_2 crystallite photocatalysts. When SiO_2 fraction is higher than 40%, the surface area and pore volume of SiO_2/TiO_2 shell, however, decrease due to the weakened reciprocal inhibition effect of volume shrinkage, thereby resulting in a decreasing tendency in MB adsorption capacity of TS50. As compared with those for Eq. (4), the higher R^2 values for Eqs. (5) and (6) suggest that pseudo-second-order and intraparticle diffusion adsorption kinetic equations are more suitable for describing the adsorption behavior of MB on SiO_2@TiO_2 crystallite photocatalysts. The plot of Eqs. (5) and (6) is shown in Fig. 6c, d. The MB adsorption on SiO_2@TiO_2 crystallite photocatalysts includes the diffusion of MB molecules from bulk solution to photocatalyst surface, intraparticle diffusion and surface adsorption. Because the pore size distribution is narrow and the tiny pores are extremely limited in the SiO_2@TiO_2 crystallite photocatalysts with lower SiO_2 fraction (10–20%), intraparticle diffusion is not rate-determining step for TS10 and TS20. However, the photocatalysts with higher SiO_2 fraction (30–50%) has a large number of tiny pores that make the intraparticle diffusion a dominating rate-determining step in adsorption process. Accordingly, the R^2 values obtained by intraparticle diffusion equation are relatively low and high for SiO_2@TiO_2 crystallite photocatalysts with lower and higher SiO_2 fraction, respectively, as compared with those obtained by pseudo-second-order equation.

Photocatalytic activity

Figure 7a, b shows the temporal changes in absorption spectra of MB solutions with representative TS0 and TS40 during UV light irradiation. With the increase of irradiation time, the absorbance of the MB solution catalyzed by TS0 gradually decreases, while that of those catalyzed by SiO_2@TiO_2 crystallite photocatalysts rapidly decreases. This means that the photocatalytic activity of TiO_2 is remarkably improved by the SiO_2 modification. The DRS analysis described above suggests that the light absorption efficiency of pure TiO_2 NPs decreases with the formation of agglomeration of TiO_2 crystalline particle. As a result, the lower photocatalytic activity of TS0 is mainly due to the serious agglomeration as well as lower MB adsorption capacity of TiO_2 NPs. Photocatalytic reaction by TiO_2 can usually be described using first-order reaction kinetic equation (Eq. 7) [34, 35].

$$\ln(C_t/C_0) = -k_1 t \quad (7)$$

where k_1 is apparent rate constant for first-order reaction, respectively.

Figure 7c, d shows the plots of C_t/C_0 and $\ln(C_t/C_0)$ against t, respectively. A good linear relationship as shown in Fig. 7d suggests that the photocatalytic degradation reaction of MB by the SiO_2@TiO_2 crystallite photocatalysts matches first-order reaction kinetics. As described above, the interaction level between SiO_2 and TiO_2, which is characterized by the change in band gap energy, is an important indicator that affects the photocatalytic activity of SiO_2@TiO_2 crystallite photocatalysts. Figure 8 shows the photocatalytic reaction rate constant (k_1), band gap energy (E_g) and absorbance (A) at $\lambda = 300$ nm as a function of the SiO_2 fraction, respectively, for SiO_2@TiO_2 crystallite photocatalysts. Both k_1 and E_g increase with the increase of SiO_2 fraction and reach their maximum values at 40% SiO_2. The surface modification of TiO_2 crystallite with SiO_2 greatly increases the interfacial area that promotes the interaction level between the counterparts. Moreover, the interaction level is further increased through the optimization of SiO_2 fraction. The enhanced interaction level characterized by the increase in band gap energy leads to the formation of more photocatalytically active centers that generate more hydroxyl radicals, thereby increasing the photocatalytic reaction rate constant (k_1). Although TS50 has the similar interaction level, it shows a relatively low activity compared with TS40 due to an excessively low fraction of TiO_2 and a decrease in

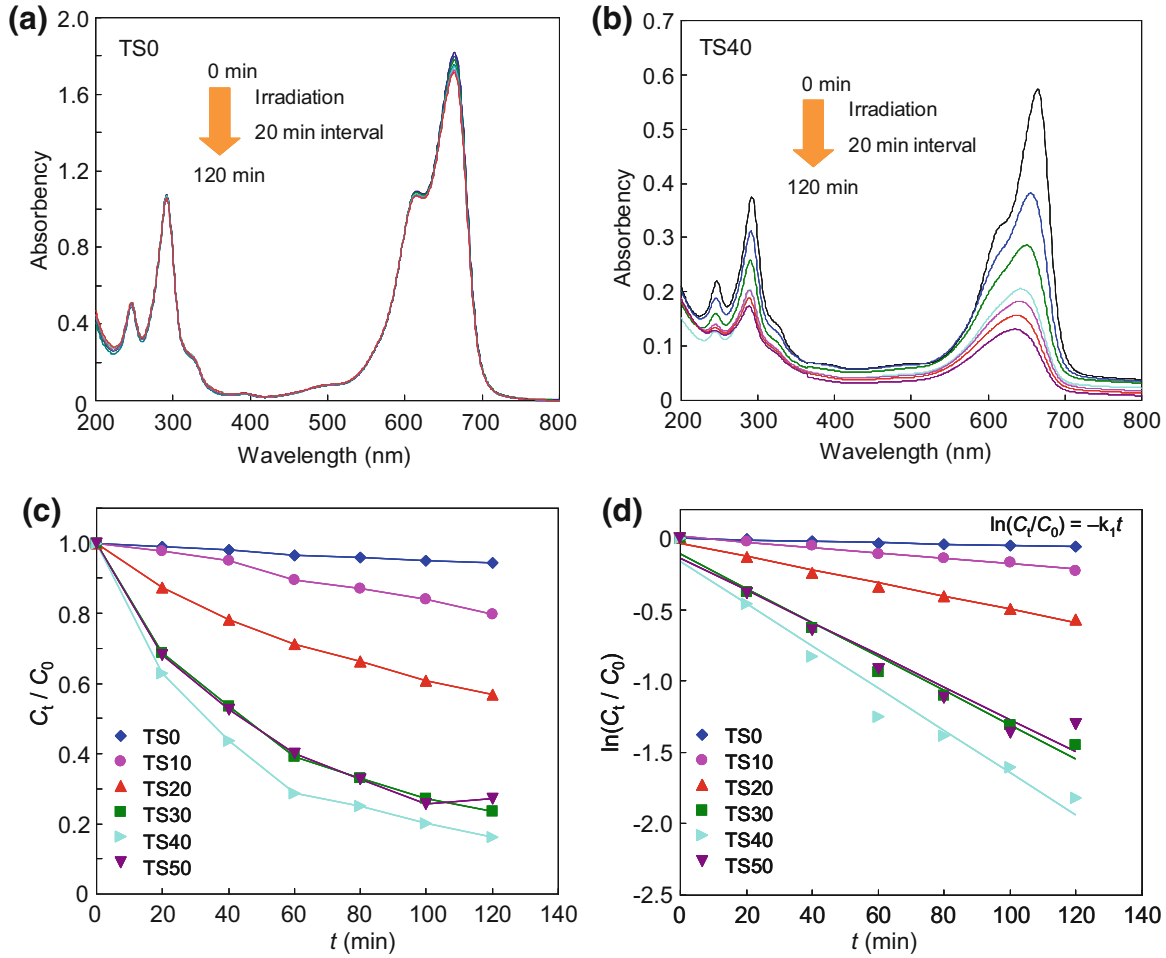

Fig. 7 Temporal changes in the absorption spectra of MB solutions with TS0 (**a**) and TS40 (**b**) during photocatalytic process and the plots of C_t/C_0 (**c**) and $\ln(C_t/C_0)$ (**d**) against t

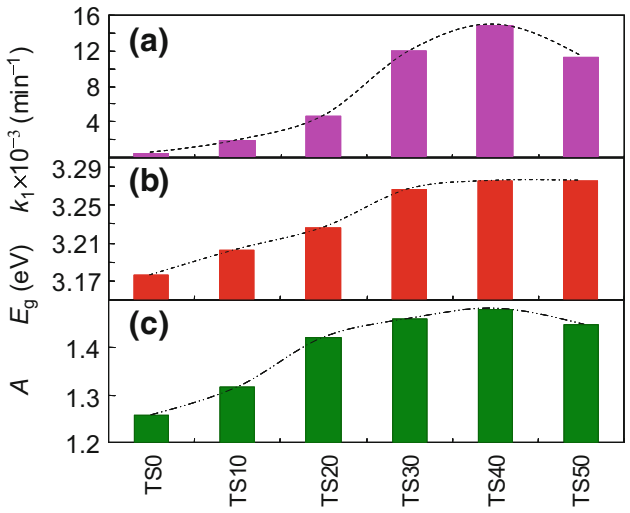

Fig. 8 Photocatalytic reaction rate constant (*a*), band gap energy (*b*) and absorbance (*c*) at $\lambda = 300$ nm measured from the corresponding DRS spectra as a function of SiO_2 fraction, respectively, for SiO_2@TiO_2 crystallite photocatalysts

adsorption capacity. Similar to k_1 and E_g, the absorbance (A) also increases with the increase of SiO_2 fraction and reaches its maximum value at 40% SiO_2. The low reflectivity of SiO_2/TiO_2 shell gives SiO_2@TiO_2 crystallite photocatalysts the merit of high utilization efficiency of incident light. In other words, the TiO_2 crystallites in SiO_2@TiO_2 crystallite photocatalysts can be regarded as the bare crystallites individually dispersed in MB solution and can thus efficiently absorb incident light even though the agglomeration of SiO_2@TiO_2 crystallite photocatalysts exists. Furthermore, SiO_2@TiO_2 crystallite photocatalysts can be easily separated from the solution by sedimentation after photocatalytic process due to the modification of SiO_2. During the adsorption process, the MB molecules in the bulk solution are adsorbed on the surface of microchannel in SiO_2/TiO_2 shell through diffusion, and then, an adsorption–desorption equilibrium of MB is established. In the subsequent photocatalytic process, the reaction of the adsorbed MB molecules with the photo-induced free as well as surface-bonded hydroxyl radicals

decreases the MB concentration at the core–shell interface and facilitates the further migration of MB molecules through the microchannels from the bulk solution toward the core–shell interface. The enrichment of MB molecules at the core–shell interface increases the capture efficiency of short-life hydroxyl radicals and thus increases the photocatalytic efficiency of SiO_2@TiO_2 crystallite photocatalysts. Consequently, the higher photocatalytic activity of TS40 is attributed to the synergistic effect of the enlarged interfacial area, enhanced interaction level, superior light absorption property as well as enlarged specific surface area of SiO_2/TiO_2 shell.

Conclusions

SiO_2@TiO_2 crystallite photocatalysts consisting of TiO_2 crystallite core and porous amorphous SiO_2/TiO_2 shell were successfully synthesized by one-pot hydrothermal process. The modification of porous amorphous SiO_2/TiO_2 on the surface of TiO_2 crystallite significantly increases the interaction level associated with the photocatalytically active center concentration and gives SiO_2@TiO_2 crystallite photocatalysts with merits of easy separation and high light absorption efficiency. The specific surface area and pore volume of SiO_2/TiO_2 shell are enlarged due to the mineralization asynchronism between the two corresponding precursors of TiO_2 and SiO_2, and thus, it promotes organic pollutant enrichment from solvent onto the surface of SiO_2@TiO_2 crystallite photocatalysts during photocatalysis process. The photocatalytic activity of SiO_2@TiO_2 crystallite photocatalysts for the degradation of methylene blue increases with the increase of SiO_2 molar fractions and reaches its maximum value at 40%SiO_2. The enhanced photocatalytic activity by SiO_2 modification is mainly attributed to the enlarged interfacial area, enhanced interaction level, superior light absorption property as well as enlarged specific surface area of SiO_2/TiO_2 shell.

Acknowledgments This work was supported by Jiangsu Key Laboratory of Advanced Catalytic Materials and Technology.

References

1. Rahimi N, Pax RA, Gray EM (2016) Review of functional titanium oxides. I: TiO_2 and its modifications. Prog Solid State Chem 44:86–105
2. Yoo SM, Rawal SB, Lee JE, Kim J, Ryu HY, Park DW, Lee WI (2015) Size-dependence of plasmonic Au nanoparticles in photocatalytic behavior of Au/TiO_2 and Au@SiO_2/TiO_2. Appl Catal A General 499:47–54
3. Zhang WJ, Bai JW (2012) Synthesis and photocatalytic properties of porous TiO_2 films prepared by ODA/sol–gel method. Appl Surf Sci 258:2607–2611
4. Xiang QJ, Yu JG, Wong PK (2011) Quantitative characterization of hydroxyl radicals produced by various photocatalysts. J Colloid Interface Sci 357:163–167
5. Wu LH, Zhou YF, Nie WY, Song LY, Chen PP (2015) Synthesis of highly monodispersed teardrop-shaped core-shell SiO_2/TiO_2 nanoparticles and their photocatalytic activities. Appl Surf Sci 351:320–326
6. Kumar SG, Rao KSRK (2017) Comparison of modification strategies towards enhanced charge carrier separation and photocatalytic degradation activity of metal oxide semiconductors (TiO_2, WO and ZnO). Appl Surf Sci 391:124–148
7. Low JX, Cheng B, Yu JG (2017) Surface modification and enhanced photocatalytic CO_2 reduction performance of TiO_2: a review. Appl Surf Sci 392:658–686
8. Abbad MMB, Kadhum AAH, Mohamad AB, Takirff MS, Sopian K (2013) Visible light photocatalytic activity of Fe^{3+}-doped ZnO nanoparticle prepared via sol–gel technique. Chemosphere 91:1604–1611
9. Song H, Li Y, Lou Z, Xiao M, Hu L, Ye Z, Zhu L (2015) Synthesis of Fe-doped WO_3 nanostructures with high visible-light-driven photocatalytic activities. Appl Catal B Environ 166:112–120
10. Yu J, Xiang Q, Zhou M (2009) Preparation, characterization and visible-light-driven photocatalytic activity of Fe-doped titania nanorods and first-principles study for electronic structures. Appl Catal B Environ 90:595–602
11. Lv XM, Zhu YH, Jiang HL, Zhong H, Yang XL, Li CZ (2014) Au@TiO_2 double-shelled octahedral nanocages with improved catalytic properties. Dalton Trans 43:15111–15118
12. Bian ZF, Tachikawa T, Zhang P, Fujitsuka M, Majima T (2014) Au/TiO_2 superstructure-based plasmonic photocatalysts exhibiting efficient charge separation and unprecedented activity. J Am Chem Soc 136:458–465
13. Meng HL, Cui C, Shen HL, Liang DY, Xue YZ, Li PG, Tang WH (2012) Synthesis and photocatalytic activity of TiO_2@CdS and CdS@TiO_2 double-shelled hollow spheres. J. Alloys Compd 527:30–35
14. Yu H, Huang X, Wang P, Yu J (2016) Enhanced Photoinduced-stability and photocatalytic activity of CdS by dual amorphous cocatalysts: synergistic effect of Ti(IV)-hole cocatalyst and Ni (II)-electron cocatalyst. J Phys Chem C 120:3722–3730
15. Wang Z, Yang C, Lin T, Yin H, Chen P, Wan D, Xu F, Huang F, Lin J, Xie X, Jiang M (2013) H-doped black titania with very high solar absorption and excellent photocatalysis enhanced by localized surface plasmon resonance. Adv Funct Mater 23:5444–5450
16. Chen X, Liu L, Huang F (2015) Black titanium dioxide (TiO_2) nanomaterials. Chem Soc Rev 44:1861–1885
17. Hurum DC, Agrios AG, Gray KA, Rajh T, Thurnauer MC (2003) Explaining the enhanced photocatalytic activity of Degussa P25 mixed-phase TiO_2 using EPR. J Phys Chem B 107:4545–4549
18. Zhao W, Zhu S, Li Y, Liu Z (2015) Three-phase junction for modulating electron–hole migration in anatase–rutile photocatalysts. Chem Sci 6:3483–3494
19. Du J, Lai XY, Yang NL, Zhai J, Kisailus D, Su FB, Wang D, Jiang L (2011) Mesoporous TiO_2 graphene composite films: improved mass transfer, reduced charge recombination, and their enhanced photocatalytic activities. ACS Nano 5:590–596
20. Thangavel S, Krishnamoorthy K, Krishnaswamy V, Raju N, Kim SJ, Venugopal G (2015) Graphdiyne-ZnO nanohybrids as an advanced photocatalytic material. J Phys Chem C 119:22057–22065
21. Gordon TR, Cargnello M, Paik T, Mangolini F, Weber RT, Fornasiero P, Murray CB (2012) Nonaqueous synthesis of TiO_2 nanocrystals using TiF_4 to engineer morphology, oxygen vacancy

concentration, and photocatalytic activity. J Am Chem Soc 134:6751–6761
22. Yu JG, Su YR, Cheng B (2007) Template-free fabrication and enhanced photocatalytic activity of hierarchical macro-/mesoporous titania. Adv Funct Mater 17:1984–1990
23. Yu JG, Zhang J (2010) A simple template-free approach to TiO_2 hollow spheres with enhanced photocatalytic activity. Dalton Trans 39:5860–5867
24. Liu JX, Wang XK, Shi F, Yu L, Liu SH, Hu SC, Liu DY (2016) Synthesis of mesoporous SiO_2 aerogel/W_xTiO_2 nanocomposites with high adsorptivity and photocatalytic activity. Adv Powder Technol 27:1781–1789
25. Cai JH, Ye YJ, Huang JW, Yu HC, Ji LN (2012) Synthesis, characterization and visible-light photocatalytic activity of TiO_2–SiO_2 composite modified with zinc porphyrins. J Sol-Gel Sci Technol 62:432–440
26. Resende SF, Nunes EHM, Houmard M, Vasconcelos WL (2014) Simple sol–gel process to obtain silica-coated anatase particles with enhanced TiO_2-SiO_2 interfacial area. J Colloid Interface Sci 433:211–217
27. Chen WH, Takai C, Khosroshahi HR, Fuji M, Shirai T (2016) SiO_2/TiO_2 double-shell hollow particles: fabrication and UV–Vis spectrum characterization. Adv Powder Technol 27:812–818
28. Mazur M, Wojcieszak D, Kaczmarek D, Domaradzki J, Song S, Gibson D, Placido F, Mazur P, Kalisz M, Poniedzialek A (2016) Functional photocatalytically active and scratch resistant antireflective coating based on TiO_2 and SiO_2. Appl Surf Sci 380:165–171
29. Li XY, He JH (2013) Synthesis of raspberry-like SiO_2-TiO_2 nanoparticles toward antireflective and self-cleaning coatings. ACS Appl Mater Interfaces 5:5282–5290
30. Xu B, Ding JE, Feng L, Ding YY, Ge FY, Cai ZH (2015) Self-cleaning cotton fabrics via combination of photocatalytic TiO_2 and superhydrophobic SiO_2. Surf Coat Technol 262:70–76
31. Levchuk I, Sillanpää M, Guillard C, Gregori D, Chateau D, Parol S (2016) TiO_2/SiO_2 porous composite thin films: role of TiO_2 areal loading and modification with gold nanospheres on the photocatalytic activity. Appl Surf Sci 383:367–374
32. Dong RL, Na C, Zhang HP, Chen ZD, Jin CC (2016) TiO_2/SiO_2 mesoporous microspheres with intelligently controlled texture. Mater Des 89:830–838
33. Langmuir I (1918) The adsorption of gases on plane surfaces of glass, mica, and platimum. J Am Chem Soc 40:1361–1403
34. Cheng WP, Gao W, Cui XY, Ma JH, Li RF (2016) Phenol adsorption equilibrium and kinetics on zeolite X/activated carbon composite. J Taiwan Inst Chem Eng 62:192–198
35. Grabowska E, Reszczyńska J, Zaleska A (2012) Mechanism of phenol photodegradation in the presence of pure and modified-TiO_2: a review. Water Res 46:5453–5471